Results in Engineering 30 (2026) 110507

Contents lists available at ScienceDirect

Results in Engineering

journal homepage: www.sciencedirect.com/journal/results-in-engineering

Research paper

Thermomechanical and isothermal fatigue behaviour of C263 nickel-based superalloy

Tomáš Vražina [a,b,*], Stefan Guth [c], Ladislav Poczklán [a,*], Jakub Poloprudský [a], Markéta Gálíková [a], Tomáš Babinský [a,d], Daniel Petrell [e], Benedikt Nowak [e], Ivo Šulák [a]

[a] Institute of Physics of Materials, Czech Academy of Sciences, Žižkova 22, 61600, Brno, Czech Republic
[b] Institute of Materials Science and Engineering, Brno University of Technology, Technická 2896/2, 61669, Brno, Czech Republic
[c] Karlsruher Institut für Technologie (KIT) Institut für Angewandte Materialien Werkstoffkunde (IAM-WK) Engelbert-Arnold-Straße, 76131, Karlsruhe, Germany
[d] Paul Scherrer Institut, PSI, Forschungsstrasse 111, 5232, Villigen PSI, Switzerland
[e] Research and Development Department, VDM Metals International GmbH, Kleffstraße 23, 58762, Altena, Germany

ARTICLE INFO

Dataset link: https://doi.org/10.5281/zenodo.1802282

Keywords:
Nickel-based superalloy
High-temperature fatigue
Dynamic recrystallisation
Dynamical strain ageing
Stacking faults

ABSTRACT

Thermomechanical fatigue (TMF) and isothermal fatigue (IF) of polycrystalline nickel-based superalloy C263 were studied. Strain-controlled fatigue experiments were conducted under in-phase and out-of-phase TMF modes in the temperature range of 300-800°C, and under high-temperature IF conditions at 800°C. The cycle duration using a triangular shape form was 100 s. The cooling/heating rate of the TMF cycle was 10°C/s. A thorough analysis of hysteresis loops was performed, and cyclic hardening/softening curves, cyclic stress-strain curves, and fatigue life curves were obtained. The presence of dynamic strain ageing and thermal recovery on the stress-strain response during TMF tests was observed. To gain insights into how temperature and strain affect the material, scanning electron microscopy and transmission electron microscopy techniques were utilised. Investigation revealed that in-phase TMF loading promoted internal intergranular damage and thus provided the lowest fatigue lifetimes across all selected strain amplitudes out of all three testing conditions. In contrast, out-of-phase TMF loading induced higher stresses and promoted transgranular fatigue crack propagation through a striation mechanism, resulting in longer fatigue lifetimes during TMF conditions. The microstructural observations revealed the occurrence of dynamic recrystallisation during TMF and IF. Fine recrystallised grains formed most prominently during TMF-OP, while TMF-IP and IF showed only localised recrystallisation near secondary cracks. This observation demonstrates that recrystallisation can be activated during cyclic TMF loading, where it influences crack propagation behaviour and can potentially reduce the lifetime of C263.

1. Introduction

In response to increasing demand to reduce fossil fuel consumption, the development of ultra-supercritical power plants represents a significant advancement in power generation sustainability. These plants operate at extremely high temperatures and pressures, exceeding the critical points of water, leading to higher thermal efficiency and, consequently, less fuel usage and lower emissions [1,2]. The durability of components used in the ultra-supercritical power plants depends not only on their long-term resistance to creep but also on their capacity to withstand short-term operational stresses, such as fluctuating loads during repeated start and stop cycles. Thermomechanical fatigue (TMF) testing simulates the complex interaction of thermal and mechanical loads that high-temperature components face, reflecting key aspects of the operational environment in ultra-supercritical power plants [3,4].

Historically, simpler and more affordable isothermal fatigue (IF) tests were often chosen over TMF tests. However, temperature cycling affects both deformation and damage mechanisms, leading to different behaviour under TMF and IF loading. According to the literature, TMF is usually more damaging than IF, even at peak operational temperatures [5–7]. Two TMF loading modes are predominantly applied across the literature [8–11], representing the most common loading scenarios. First is the in-phase mode (IP), where maximum temperature coincides with maximum strain, and therefore, the phase angle between strain and temperature is 0°. The second typical TMF loading mode is out-of-phase (OP), in which the temperature and deformation have a phase shift of

* Corresponding authors.
E-mail addresses: vrazina@ipm.cz (T. Vražina), poczklan@ipm.cz (L. Poczklán).

https://doi.org/10.1016/j.rineng.2026.110507
Received 4 January 2026; Received in revised form 21 March 2026; Accepted 9 April 2026
Available online 10 April 2026

180°, meaning that the maximum temperature coincides with the minimum strain, and vice versa. The TMF-IP cycle is linked to conditions of cold spots, where the local temperature is lower than that of the surrounding material. Conversely, the TMF-OP cycle corresponds to hot spots, where the temperature exceeds that of the adjacent areas. Cold spots are, e.g., found near the turbine blade's cooling channels, whereas hot spots are often located on the blade's aerofoil or platform [12].

Depending on the phase angle, significant variations can occur in the micromechanical behaviour, especially in the formation of dislocation structures and in crack initiation and propagation [8,13]. Prasad Reddy et al. [14] noted that below a certain temperature (different for each material), transgranular crack propagation mechanisms prevail. As the maximum temperature increases, crack growth shifts toward intergranular mechanisms [15]. Research on polycrystalline materials [16–19] revealed that under TMF-OP conditions, cracks propagate predominantly transgranularly, while under TMF-IP conditions, crack propagation is mainly intergranular, and in some instances, the creep cavities are present and contribute to intergranular propagation [20].

Components operating in ultra-supercritical power plant units are subjected to harsh environments during TMF, which demands the use of materials capable of enduring the severe nature of this environment. In this context, various materials such as Alloy 740, Alloy 617, or the polycrystalline precipitation hardened nickel-based superalloy C263 were considered for selected components of ultra-supercritical power plants. Specifically, Alloy C263 has been identified as a suitable material for steam pipe components [18,21–23] and has found applications in transition liners, exhaust systems, and casings of aircraft engines [18,24,25].

A lot of effort was put into exploring the isothermal low-cycle fatigue behaviour of C263 since the early 21st century [18,23,26–28]. Various IF tests in the temperature range starting at room temperature up to 950°C were performed. Jadav et al. [26] conducted IF testing at temperatures of 25°C, 450°C, and 650°C, while Dinesh's most recent studies describe high-temperature damage mechanisms during low-cycle fatigue of Superni SU-263 at 750°C [29], 800°C, 850°C, and 900°C under different strain amplitudes [30]. Both Jadav et al. [26] and Dinesh et al. [29,30] reported the occurrence of dynamic strain ageing (DSA) at higher temperatures. The DSA effect is often characterised by serrations observed on hysteresis loops. DSA involves diffusing solute atoms interacting with dislocations, impeding their movement until sufficient stress causes a dislocation to break free, resulting in a plastic strain burst and a concomitant stress drop [13,31,32].

There is very limited literature available regarding the TMF performance of C263 superalloy [18,22,24]. Manonukul et al. [24] conducted three strain-controlled TMF tests: one in-phase test over 300–800 °C, one in-phase test over 300–950 °C, and one out-of-phase test over 300–950 °C, all with a strain amplitude 0.3% to examine behaviour above and below the γ′ solvus and to validate a combined creep–cyclic plasticity model. Bhattachar [22] conducted TMF tests on C263 sheet specimens. Zhang [18] performed strain-controlled TMF-IP and TMF-OP tests along with IF tests. However, only with a single strain amplitude for each mode and with a temperature range peaking at 950 °C, which surpasses the maximum temperature of 850°C recommended by manufacturers [33]. The current study addresses these gaps by presenting data from TMF tests with a service-near temperature range of 300-800°C, typical for exhaustion liners [34], and with various strain amplitudes. Life curves under both TMF-IP and TMF-OP conditions are derived alongside the IF tested at 800°C as a reference. The study also further examines the microstructure and fractography to elucidate the links between TMF testing and the resultant microstructural configurations, thereby enhancing the understanding of the material's behaviour under operational conditions.

2. Materials and methods

2.1. Material

The investigated material in this study is the polycrystalline precipitation hardened nickel-based superalloy C263. VDM Metals International GmbH supplied the raw material as a hot-rolled plate. The heat treatment involved solid solution annealing at 1200 °C for 1 hour, followed by precipitation hardening at 800°C for 8 hours in air. The nominal chemical composition of C263 alloy, as provided by the manufacturer, is presented in Table 1.

Cylindrical specimens, as schematically shown in Fig. 1a, with a gauge length diameter of 7 mm, were machined from a C263 hot-rolled plate. Subsequently, the surface of the gauge length was ground and electrolytically polished to allow for observation of evolving surface relief as depicted in Fig. 1b. The cylindrical specimen geometry was selected in accordance with the Validated Code-of-Practice for Strain-Controlled Thermo-Mechanical Fatigue Testing [35].

2.2. High-temperature fatigue testing

The TMF tests were controlled with total strain amplitude consisting of the desired mechanical strain course added to thermal strain recorded during thermal cycling at zero stress. Recording thermal strain is not necessary for isothermal testing. Therefore, the IF tests were controlled directly with total mechanical strain amplitude. The mechanical strain amplitudes (in %) used were 0.5, 0.4, 0.35, and 0.3 for TMF-IP tests; 0.6, 0.5, 0.4, and 0.35 for TMF-OP tests; and 0.7, 0.5, 0.4, and 0.35 for IF tests. The amplitudes were chosen to keep the lifetime in the low-cycle region. Different damage mechanisms in TMF-IP, TMF-OP, and IF can lead to different fatigue lives at the same strain amplitude. Therefore, the amplitudes were adjusted during design to achieve overlapping lifetime regimes for meaningful comparison across loading modes. The strain was measured with a high-temperature extensometer with alumina rod extensions. Heating of specimens was achieved through an induction system with a water-cooled copper coil. Cooling was realised by the thermal conduction of the water-cooled grips, supplemented by additional air-cooling jets, achieving a cooling rate of 10°C/s. The heating rate was also kept at 10°C/s. The tests involved uniaxial, fully reversed (R=-1) cycling with a triangular waveform. The temperature span for TMF tests was set between 300-800 °C, with IF tests carried out at the maximum temperature of the TMF cycle of 800°C. Each cycle lasted 100 seconds, divided equally between the heating and cooling phases. The same cycle period was applied to the IF tests. The TMF tests encompassed two distinct loading cycles, as illustrated in Fig. 2, namely TMF-IP and TMF-OP, to simulate different operational conditions.

Temperature uniformity across the specimen was ensured by employing three ribbon-type NiCr-Ni thermocouples (type K), which were placed at the centre and both ends of the gauge length. The number of cycles to failure was defined as the number of elapsed cycles when the criterion given by Eq. 1:

$$\frac{\left(\sigma^{i}_{\max} - \sigma^{i}_{\min}\right) - \sigma^{ref}_{a}}{\sigma^{ref}_{a}} \leq 0.7 \tag{1}$$

was met, or at the time of fracture, before the criterion was fulfilled. The σ_{max} and σ_{min} are the maximum and minimum stress in the i-cycle, and σ_a is a reference stress amplitude set at the 10^{th} cycle. The value of 0.7 correlates approximately to the fatigue crack spread over half of the specimen circumference [8].

Table 1
Chemical composition of C263 alloy specified by the manufacturer.

Element	Cr	Fe	C	Si	Mo	Co	Al	Ti	Ni
Wt. %	19.9	0.6	0.05	0.2	5.8	19.7	0.5	2.1	Bal.

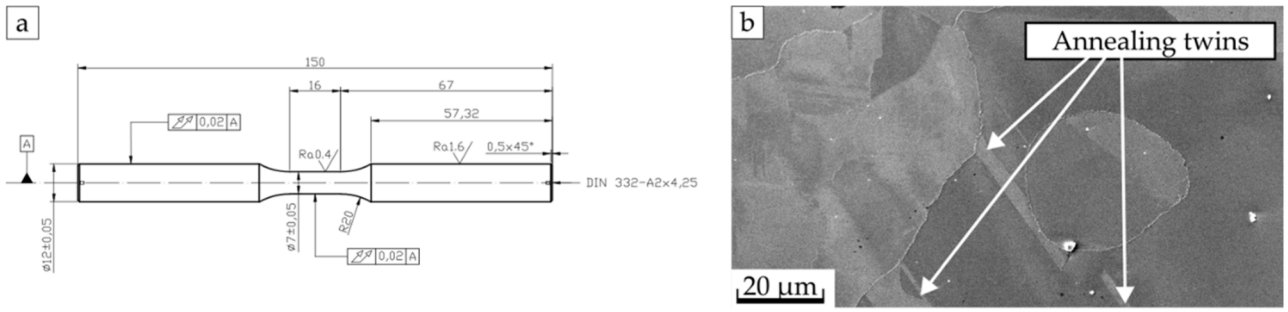

Fig. 1. (a) Schematic drawing of the cylindrical fatigue specimen used for TMF and IF testing, lengths in mm; (b) smooth surface of C263 alloy treated by electrolytic polishing with observable polyhedral grains and annealing twins.

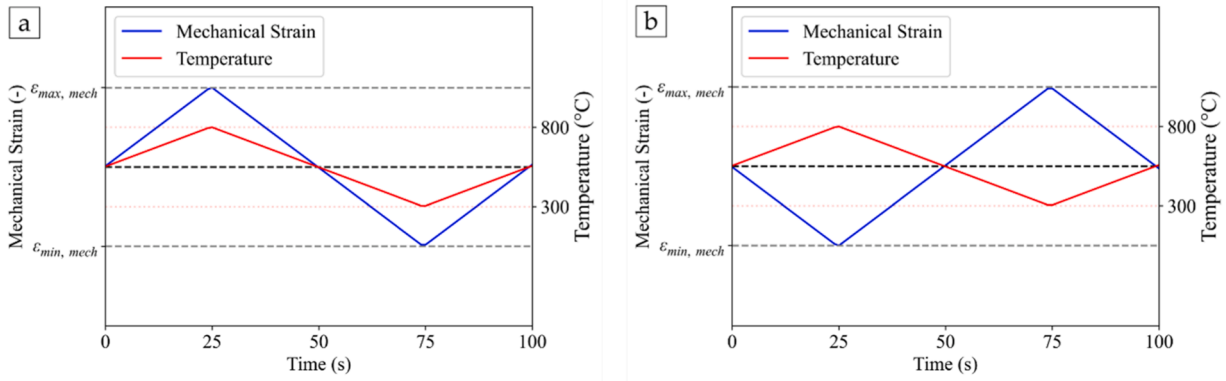

Fig. 2. Thermomechanical Loading cycles (Strain/time dependence) during (a) TMF-IP; (b) TMF-OP.

2.3. Observation

The surface topography of the fatigued specimens was examined to investigate the impact of different loading conditions on crack initiation. Following this, the specimens were fractured into two halves (had they not already fractured during the fatigue test) for further analysis. From each of the halved cylindrical specimens, one segment was allocated for detailed fractographic analysis. The counterpart segment was divided into three distinct sections: one dedicated to X-ray Diffraction (XRD) analysis, another reserved for comprehensive microstructural and Electron Backscatter Diffraction (EBSD) observations, and the central segment arranged for in-depth Transmission Electron Microscopy (TEM) analysis. The metallographic sections for EBSD analysis were prepared by grinding on SiC papers and polishing by diamond suspensions, followed by electrolytic polishing in a solution composed of $HNO_3 + HClO_4 + C_2H_5OH$ in a volume ratio of 1:3:66. A LYRA 3 XMU FEG/SEMxFIB scanning electron microscope (SEM), equipped with an Oxford Instruments X-MAX 80 energy-dispersive spectrometer (EDS) and an Oxford Instruments Symmetry EBSD detector, was used to examine the microstructure, analyse damage mechanisms, and the fracture surfaces of the specimens. Grain size was determined from EBSD maps using the AZtecCrystal software, adopting the equivalent circle diameter method, with a misorientation threshold set at 15°. Utilising the EBSD detector, examinations were conducted over an area measuring $1500 \times 2000\ \mu m^2$. In-depth TEM analysis of dislocation structures was carried out by a JEOL JEM-2100F, which is equipped with a bright field detector and a high-angle annular-dark field detector, enabling detailed observations in scanning transmission electron microscopy (STEM) mode. The selected area electron diffraction patterns were acquired using a Thermo Scientific Talos F200i. For the evaluation of dislocation density in fatigued samples, the local foil thickness was determined from convergent beam electron diffraction (CBED) patterns acquired in STEM mode. To verify the measured crystallographic distances, X-ray powder diffraction was employed. Diffraction patterns were collected in a 2θ range from 30° to 120° with a step size of approximately 0.05°, using Bragg-Brentano geometry in reflection mode on a PanAnalytical Empyrean diffractometer equipped with a Co Kα X-ray source.

3. Results

3.1. Initial state

The microstructure of the investigated C263 superalloy consists of a matrix formed by a face-centred cubic γ-phase $M_{23}C_6$ carbides (Fig. 3a), MC-type carbides (Figs. 3a, b) and coherent γ' precipitates (Fig. 3c). Carbides of the $M_{23}C_6$ type, where M is typically Cr and Mo, decorate grain boundaries (Fig. 3a). These carbides were not observed outside grain boundaries, in contrast to MC carbides. MC carbides, where M corresponds to elements Mo and Ti (Figs. 3a, b), can be found either as sharp particles with sizes ranging from 100 to 400 nm (Fig. 3b) or as finely dispersed phases along the grain boundaries (Fig. 3a). A characteristic feature of MC carbides is the local depletion of Ti in the surrounding matrix and therefore no γ′ can be observed in the vicinity of these carbides. This depletion is evident in both Fig. 3a and Fig. 3b. The γ′ nanoprecipitates range from 10 to 30 nm in size and are uniformly distributed within the matrix. Elemental maps confirm an increased concentration of Ni, Al, and Ti within the γ' precipitates (Fig. 3c), whereas Co and Cr are concentrated in the channels between the precipitates (Fig. 3c). Stacking faults were observed in the initial state of the material, as shown in Fig. 3d, as well as a negligible number of dislocations. The C263 superalloy predominantly consists of polyhedral grains, though the IPF-coloured EBSD map (Fig. 3e) also reveals grains elongated along the rolling direction. However, these grains are rather isolated, and the structure does not show significant hot-rolling artefacts such as flattened grains. The IPF images (Fig. 3f) indicate a weak crystallographic texture, with a maximum texture intensity of 2.44 multiples

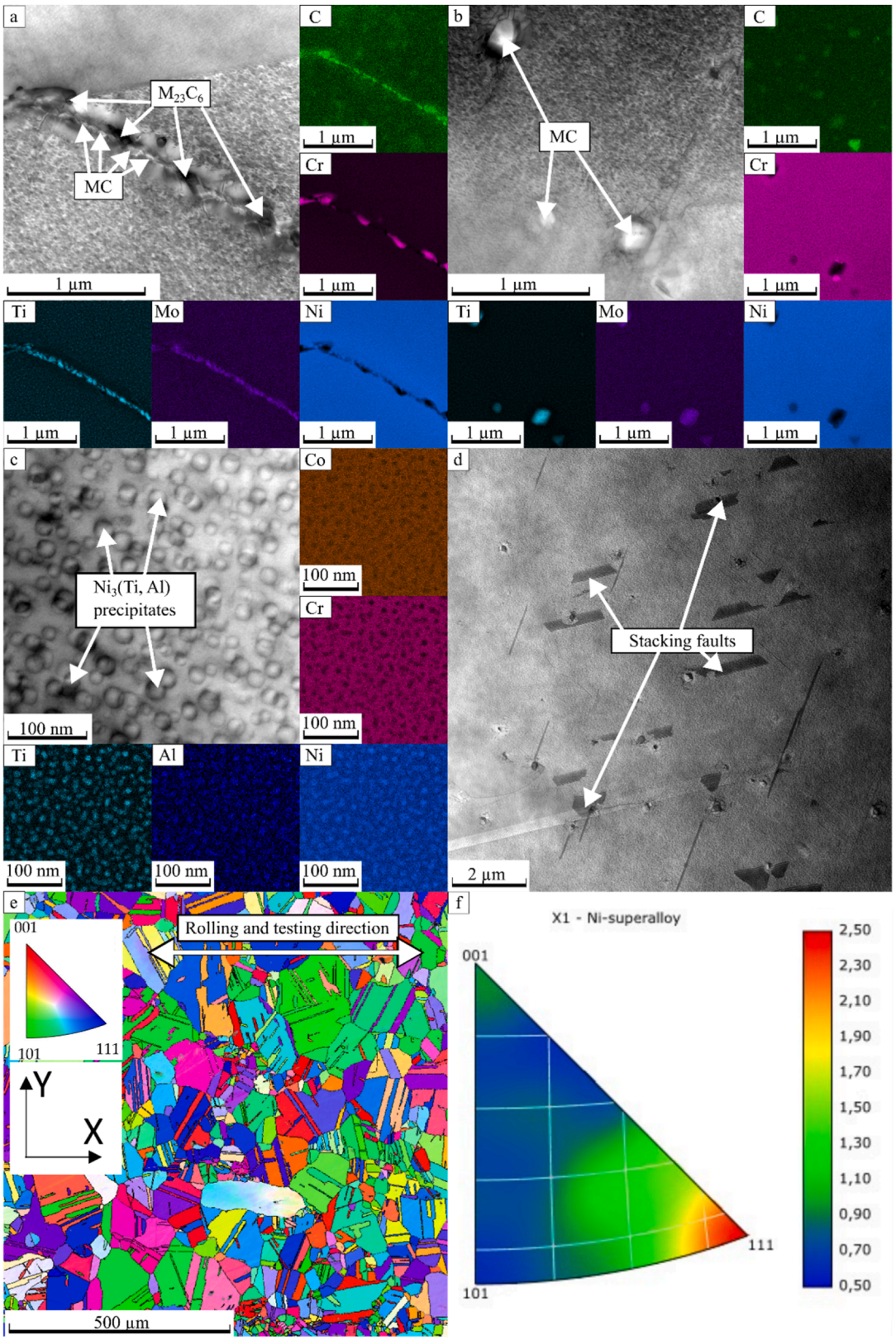

Fig. 3. Microstructural characterisation of C263 nickel-based superalloy (a) STEM micrograph of grain boundary with EDS maps highlighting MC and $M_{23}C_6$ carbides; (b) STEM micrograph with EDS maps of matrix with MC carbides; (c) detail of spherical precipitates γ' with corresponding EDS maps; (d) STEM micrograph of stacking faults; (e) EBSD grain orientation macrograph of bimodal distribution of grain size; (f) IPFX images.

of uniform distribution (MUD). The material contains numerous annealing twins, which are characteristic of recrystallisation during annealing in low stacking fault energy materials, such as alloy C263. Within individual grains, both complete and incomplete annealing twins can be observed, featuring both coherent and incoherent boundaries. The average grain size is 50 μm ± 49 μm.

3.2. Lifetime results

Fig. 4a displays the relationship between total mechanical strain amplitude ($\varepsilon_{a,\ mech}$) and fatigue lifetimes (N_f) of samples under TMF-IP, TMF-OP, and IF loading. The results are compared with findings from IF studies with lower cycle periods performed by Zhang and Knowles [18] and Dinesh et al. [30]. The total mechanical strain was chosen for each loading mode to achieve a similar range of lifetimes, with $\varepsilon_{a,\ mech}$ of 0.5% and 0.4% applied for all testing conditions. The TMF-IP mode emerged as the most detrimental, exhibiting the shortest lifetimes. However, as the $\varepsilon_{a,\ mech}$ decreases, the curves approach each other, and at low strain amplitudes, the IF fatigue curve intersects with the TMF-IP curve, showing similar lifetimes. The IF lifetime curve reported by Dinesh et al. [30] exhibits a slightly lower slope and generally higher lifetimes than the IF tests conducted in this study; with both trends intersecting at very high strain amplitudes. The IF curve from Zhang and Knowles [18] differs significantly from both aforementioned life curves, as it has a considerably different slope, and the fatigue lifetimes lie between those of TMF-OP and TMF-IP tests from this study. Taking into account the inherent statistical variance of the fatigue data, combining the data from [18,30] can produce a single IF life curve that exhibits a higher fatigue life than any of the data obtained in this work. Fig. 4b depicts the relationship between plastic strain amplitude (evaluated as half of the width of the hysteresis loop at mean stress levels) at half of the lifetime against the number of cycles until fracture using a bilogarithmic scale, with the experimental data fitted according to Eq. (2). In this Eq., ε_f' represents the fatigue ductility coefficient, and c is the fatigue ductility exponent. Original data in Fig. 4b are supplemented by the Manson coffin curve from literature [30]. The coefficients estimated through a least squares method, based on Eq. (2), are presented in Table 2. There is a clear order of lifetimes (TMF-IP<TMF-OP<IF) in the Manson-Coffin plot, while for the total mechanical strain amplitude, the curves intersect and appear to unite at lower amplitudes. Fig. 4c depicts the relationship between stress amplitude and the number of cycles until fracture. In Fig. 4c, the order of lifetime is IF<TMF-IP<TMF-OP. The coefficients for the Basquin curve are estimated in Table 2 based on Eq. (3). Both Eqs. (2) and (3) were evaluated using parameters obtained from the hysteresis loop at half of the fatigue lifetime, which represents the stabilised cyclic response.

$$\log\varepsilon_{a,\ pl} = c\log(2N_f) + \log\left(\varepsilon_f'\right) \tag{2}$$

$$\log\sigma_a = b\log(2N_f) + \log\left(\sigma_f'\right) \tag{3}$$

Table 2
Calculated parameters for Manson Coffin fatigue curves of C263 superalloy under IF and TMF loading. (*recalculated).

Parameter	IF	TMF-IP	TMF-OP	IF [30]
$\varepsilon_f'(-)$	0.46	0.32	0.19	0.49
c (-)	-0.71	-0.83	-0.68	-0.72
σ_f' *(MPa)*	14675	1092	2663	1367*
b (-)	-0.52	-0.10	-0.19	-0.11*

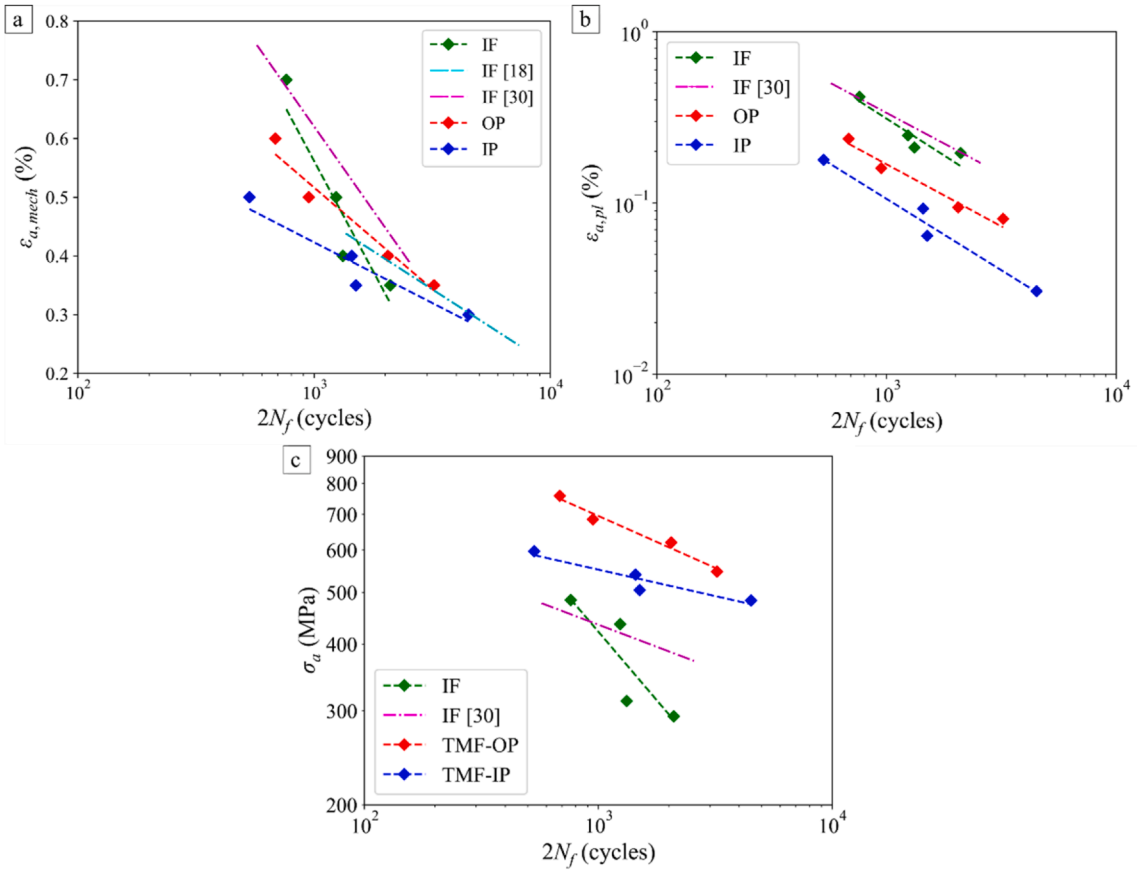

Fig. 4. Fatigue life curves of C263 nickel-based superalloy cycled under IF, TMF-IP, and TMF-OP conditions (a) mechanical strain amplitude vs number of cycles to failure; (b) Manson-Coffin representation; (c) Basquin representation.

3.3. Cyclic deformation behaviour

Fig. 5 shows stress-strain hysteresis loops recorded in the first, tenth cycle, and at half of the fatigue life ($N_f/2$). In the high-temperature part of a cycle, the maximum/minimum stress ($\sigma^i_{max}/\sigma^i_{min}$) is reached before the maximum/minimum strain value ($\varepsilon^i_{max}/\varepsilon^i_{min}$) of a strain-controlled IP TMF and OP TMF cycle, respectively (Fig. 5a, Fig. 5b). The phenomenon is typical for TMF and related to increasing temperature and thus decreasing resistance of the material to imposed stress. This is caused by incipient creep mechanisms activated at elevated temperatures, sometimes referred to as dynamic relaxation. Serrated flow is observed in the low-temperature part of the cycle regardless of the phase shift. In the case of the TMF-IP cycle, the serrated plastic flow occurred in the compression segment of the hysteresis loop, as shown in Fig. 5a. Conversely, under TMF-OP loading, the serrations were present in the tensile part of the hysteresis loop. Serrated plastic flow is not observed under IF loading (Fig. 5c) and at low strain amplitudes. During TMF cycling, the hysteresis loops shift along the stress axis; reflecting the evolution of mean stress (σ_m) toward compressive values under the TMF-IP case (see Fig. 5a, d – dashed lines), and towards the tensile regime in the OP (see Fig. 5b – dashed lines) case.

Table 3 outlines the cycle count at which the serrated plastic flow ceases. It shows that serrated plastic flow, defined by stress drops greater than 5 MPa [10], occurs in every cycle until failure for $\varepsilon_{a,\ mech}$ greater than 0.5%. As $\varepsilon_{a,\ mech}$ decreases, the serrated plastic flow starts to fade away after fewer cycles. Under TMF-IP loading with $\varepsilon_{a,\ mech}$= 0.3% serrated yielding is not manifested at all, which corresponds to Fig. 5d.

The relationship between σ_a and cycle number is depicted in Fig. 6. Fig. 6a and Fig. 6b illustrate that the degree of hardening in TMF-IP and TMF-OP cycles is substantially greater than during isothermal fatigue (Fig. 6c). Among all conditions at the same strain amplitude levels, TMF-OP exhibits the highest stress amplitudes, followed by TMF-IP and IF cycles.

Table 3
The occurrence of serrated plastic flow under TMF loading for various mechanical strain amplitudes. The values for plastic strain amplitude $\varepsilon_{a,\ pl}$ and stress amplitude σ_a correspond to the cycle at half of the lifetime.

Loading mode	$\varepsilon_{a,\ mech}$ (%)	$\varepsilon_{a,\ pl}$ (%)	σ_a (MPa)	N_f (-)	Last cycle showing serrated flow in T=300-400°C
TMF-IP	0.5	0.18	597	266	N_f
TMF-IP	0.4	0.09	540	721	221
TMF-IP	0.35	0.06	505	751	102
TMF-IP	0.3	0.03	483	2249	n/a
TMF-OP	0.6	0.23	758	342	N_f
TMF-OP	0.5	0.16	685	474	N_f
TMF-OP	0.4	0.09	620	1025	360
TMF-OP	0.35	0.08	547	1608	118
IF	0.7	0.42	484	381	n/a
IF	0.5	0.25	436	619	n/a
IF	0.4	0.21	313	661	n/a
IF	0.35	0.20	293	1050	n/a

Both TMF-IP and TMF-OP cycling lead to a similar stress amplitude development consisting of an initial strengthening followed by saturation, after which it decreases due to incipient cracking. In IF cycles, there is initial hardening within the first few cycles, followed by a gradual softening until crack initiation.

Cyclic stress-strain curves showing the dependence between σ_a and ε_{ap} can be seen in Fig. 7. The plot highlights the significant decrease in σ_a for IF-tested samples, corresponding to the cyclic softening observed in Fig. 6c. Additionally, the IF-tested samples exhibit a notably higher ε_{ap} than those tested under TMF conditions. Experimental data are fitted with the following Eq. (3), where K' represents the fatigue hardening

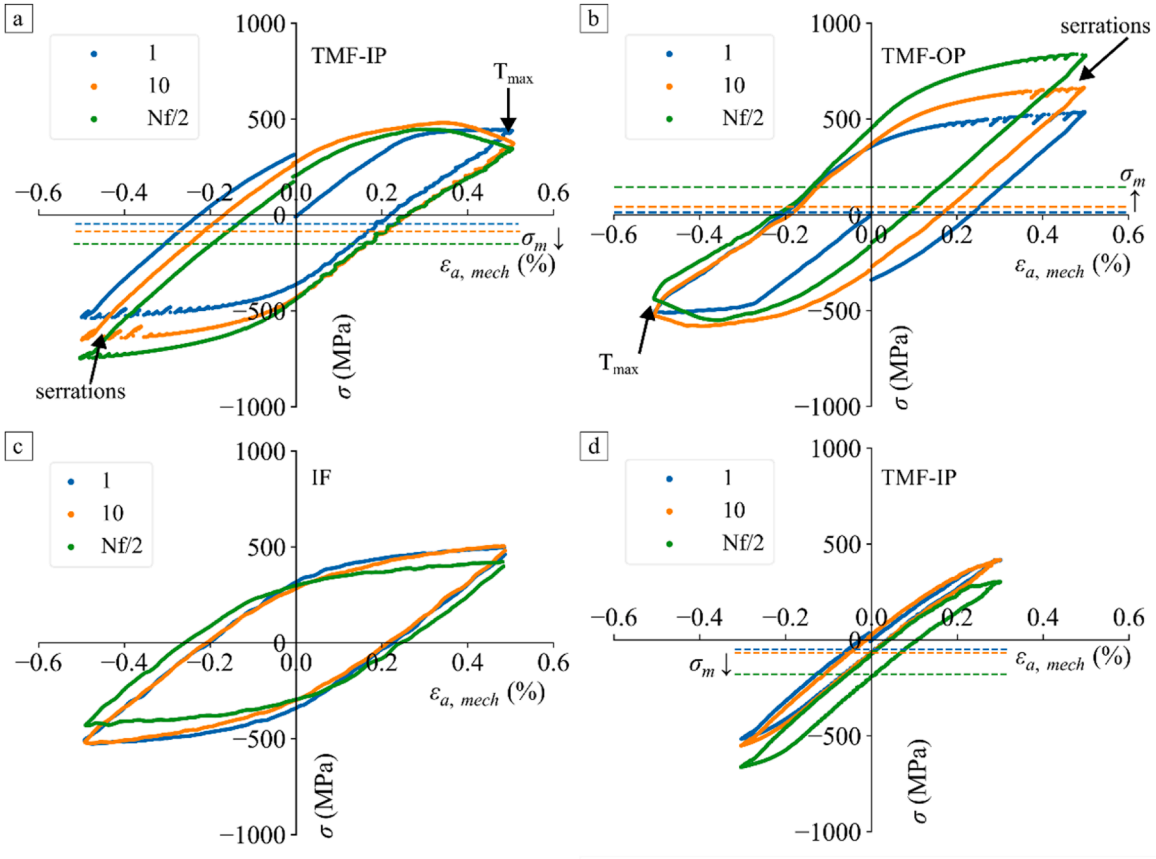

Fig. 5. Recorded hysteresis loops for 1st, 10th, and $N_f/2$ cycles of C263 alloy loaded under (a) TMF-IP with $\varepsilon_{a,\ mech}$ = 0.5%; (b) TMF-OP with $\varepsilon_{a,\ mech}$ = 0.5%; (c) IF with $\varepsilon_{a,\ mech}$ = 0.5%; (d) TMF-IP with $\varepsilon_{a,\ mech}$ = 0.3%.

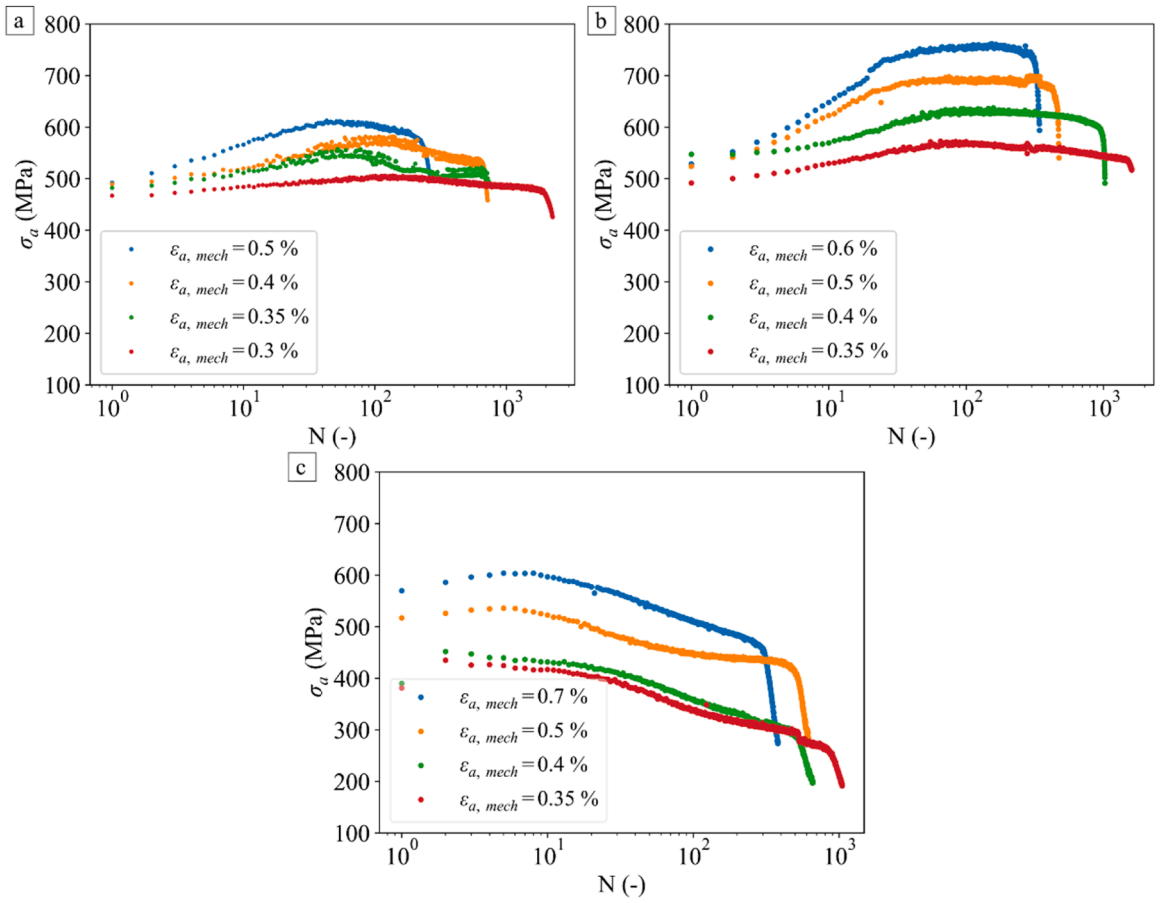

Fig. 6. Softening/hardening curves in conditions of (a) TMF-IP; (b) TMF-OP; (c) IF.

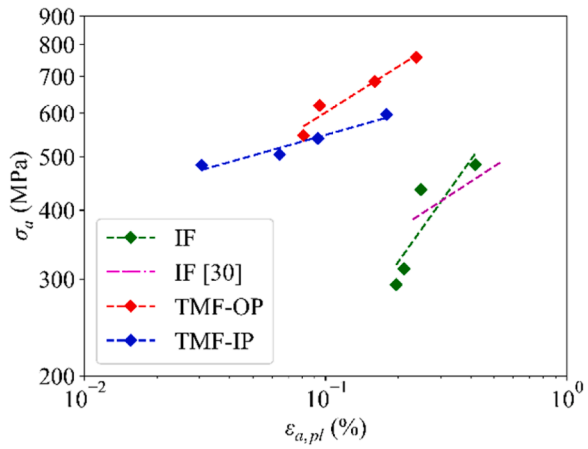

Fig. 7. Cyclic stress-strain curves of C263 cycled in conditions of TMF-IP, TMF-OP, and IF.

coefficient of the cyclic stress-strain curve, and n' is the fatigue hardening exponent of the cyclic stress-strain curve. The parameters of this dependence for specimens tested at TMF-IP, TMF-OP, and IF conditions are shown in Table 4.

Table 4
Calculated parameters for cyclic stress-strain curves of C263 superalloy (recalculated*).

Parameter	IF	TMF-IP	TMF-OP	IF [30]
K (MPa)	16596	1271	4039	2156*
n´(-)	0.64	0.12	0.28	0.28*

$$\log\sigma_a = n'\log\left(\varepsilon_{ap}\right) + \log\left(K'\right) \quad (4)$$

3.4. Fractographic analysis

Fig. 8 presents the fracture surfaces of cyclically strained C263 superalloy under TMF-IP (Fig. 8a-c), TMF-OP (Fig. 8d-f), and IF (Fig. 8g-i) loading conditions. The fracture surfaces observed after IF and both TMF loadings display multiple crack initiation sites originating from the specimen surface, as illustrated by the overview images in Fig. 8a, d, and g. Under TMF-IP loading (Fig. 8b), the fracture surface exhibits clear intergranular crack propagation, as indicated by the presence of grain boundary facets and a secondary crack propagating between them. In contrast, the TMF-OP specimen (Fig. 8e) shows predominantly transgranular fatigue cracking, characterised by well-defined striations. Deformation twins are visible in the microstructure shown in Fig. 8f. For the IF condition, both transgranular cracking with visible striations (Fig. 8h) and intergranular crack propagation (Fig. 8i) are observed, suggesting a mixed-mode fatigue fracture mechanism. The corresponding EBSD maps for TMF-IP (Fig. 8c), TMF-OP (Fig. 8f), and IF (Fig. 8i), taken from longitudinal sections (parallel to loading direction within the gauge length), reveal areas of dynamic recrystallisation with very fine grains (<1 μm) formed along the boundaries of larger grains (50–200 μm). Although the TMF-OP specimen exhibits mainly transgranular cracking (Fig. 8f), there are local transitions to intergranular cracking, likely promoted by the presence of fine grains, similar to the behaviour observed under IF loading (Fig. 8i).

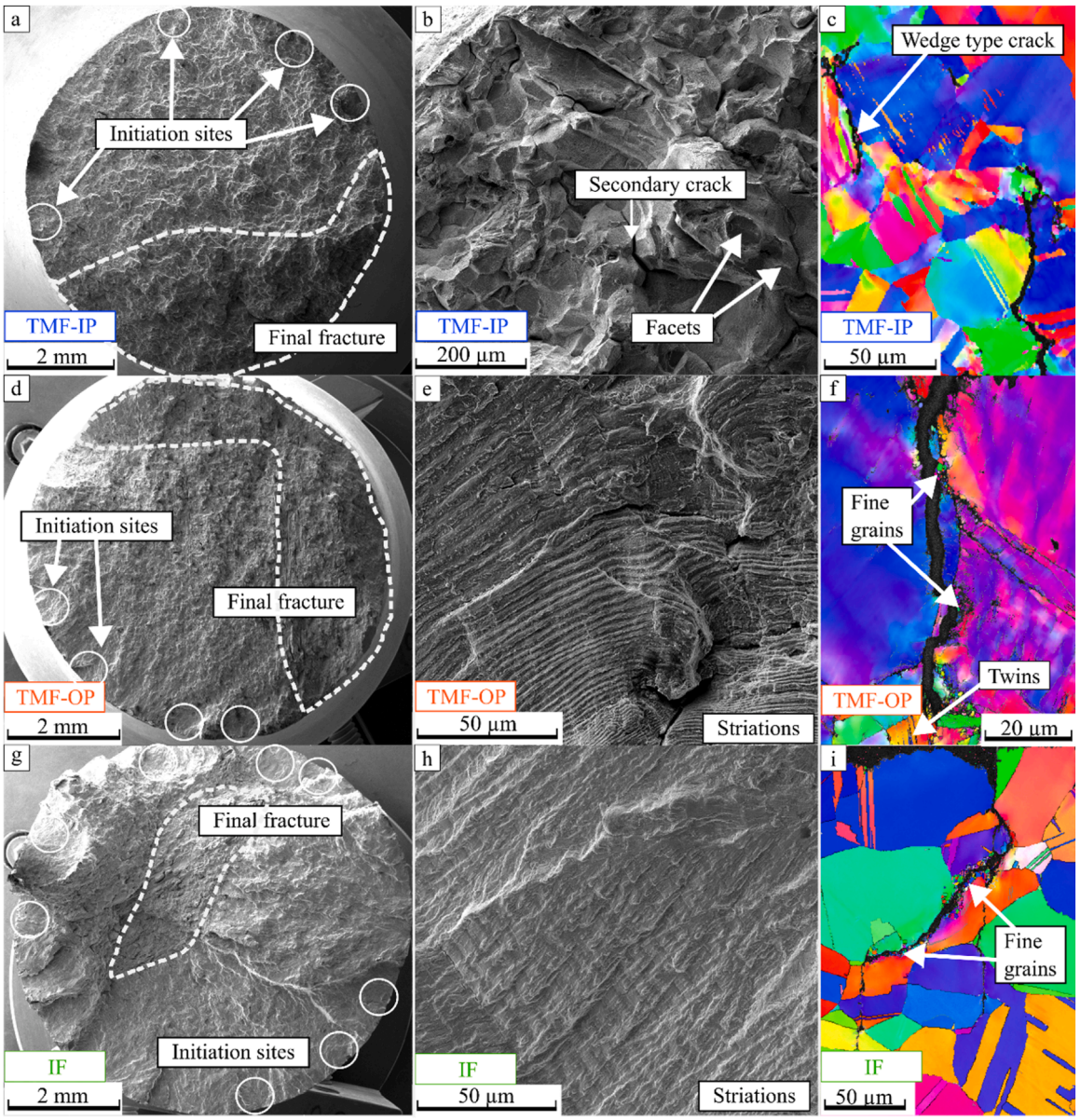

Fig. 8. Fractographical analysis of samples tested with $\varepsilon_{a,\ mech} = 0.5\%$ (a) Fractured surface after exposure to TMF-IP loading; (b) detail of the fracture surface from Fig. 8a; (c) EBSD map of the longitudinal section of the TMF-IP loaded specimen; (d) fractured surface after exposure to TMF-OP loading; (e) detail of the fracture surface from Fig. 8d; (f) EBSD map of the longitudinal section of the TMF-OP loaded specimen; (g) fractured surface after exposure to IF loading; (h) detail of the fracture surface from Fig. 8g; (i) EBSD map of the longitudinal section of the IF loaded specimen.

3.5. Microstructural analysis

The internal microstructure of specimens subjected to TMF-IP captured via TEM is illustrated in Fig. 9a-c. Fig. 9a shows the occurrence of micro-twins, further proved by the selected area electron diffraction (SAED) pattern. Micro-twins were not observed in the initial state but predominantly appeared in materials tested under TMF-IP and TMF-OP conditions, indicating their formation during testing. The predominant mechanism of dislocation interaction with fine Ni_3(Ti, Al) precipitates is identified as dislocation bowing, a typical strengthening mechanism in alloys with precipitates, showcased in Fig. 9a and b. This mechanism was similarly observed in specimens after TMF-OP loading, shown in Fig. 9e and f. In Fig. 9d, the dislocations that formed during TMF-OP testing organise into a substructure, indicating a significantly elevated dislocation density in specimens cycled under TMF-OP conditions. A characteristic feature observed in TMF-OP specimens is the formation of dislocation tangles, closely examined in Fig. 9e.

Although infrequent, some stacking fault tetrahedra are present, as seen in Fig. 9f. In contrast, the IF-tested samples exhibited a completely different dislocation structure, primarily consisting of stacking faults (Fig. 9g, i) aligned along {111} slip planes and single dislocation lines bowing or bypassing Ni_3(Ti, Al) precipitates, as depicted in Fig. 9h, i. Following all the loading cycles at $\varepsilon_{a,\ mech} = 0.5\%$, the size difference of the Ni_3(Ti, Al) precipitates is insignificant in comparison to the reference state (Fig. 3c).

Persistent slip bands (Fig. 8f) were observed in both TMF-IP and TMF-OP loaded samples. The main difference is in the distribution and density of dislocations and, therefore, the size of slip bands. Fig. 10 displays representative micrographs for all three loading conditions captured at two total mechanical strain amplitudes, 0.5% and 0.35%: TMF-IP (Fig. 10a, d), TMF-OP (Fig. 10b, e), and IF (Fig. 10c, f). The corresponding dislocation densities were measured using the method described in [36], and the thickness of the TEM foil was obtained from the CBED pattern by the two-beam condition, as reported in [37]. The

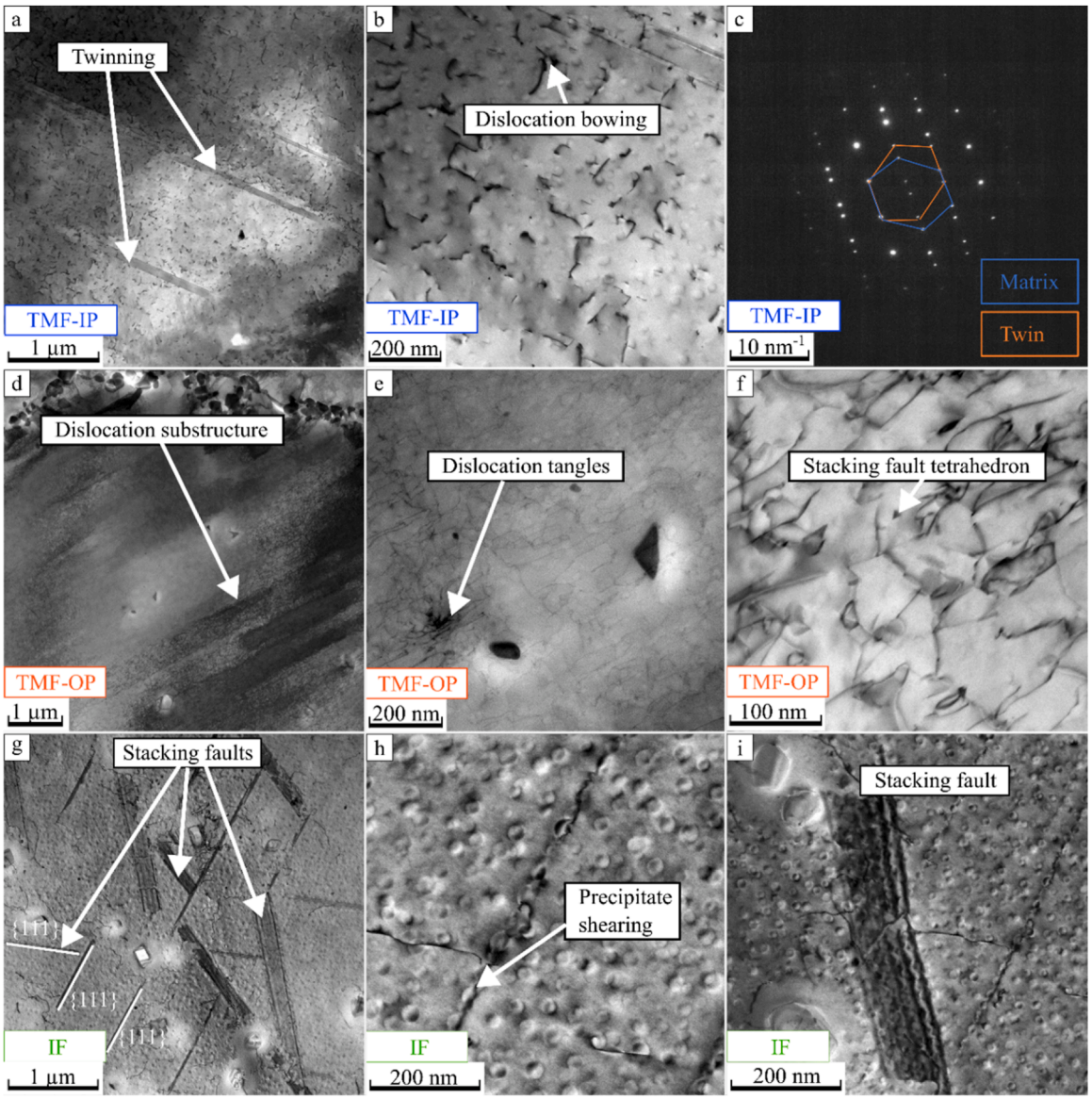

Fig. 9. STEM micrographs of micro- and nanostructural features observed in samples loaded with $\varepsilon_{a,\ mech} = 0.5\%$:(a) Deformation twins;(b) Detail of dislocation interaction; (c) SAED pattern of twins; (d) Dislocation substructure; (e) Dislocation tangles; (f) Stacking fault tetrahedron; (g) Multiple stacking faults; (h) Interaction of dislocation with precipitate; (i) Detail of stacking fault.

dislocation density (DD) was evaluated using three separate micrographs for each loading condition. In each image, dislocations were quantified by counting their intersections with a grid of five vertical and five horizontal lines. The highest dislocation density of all three loading conditions was measured in TMF-OP, and the lowest in the IF tested specimens. In IF-tested specimens, the Shockley partials originally forming the stacking fault under cyclic straining with $\varepsilon_{a,\ mech} = 0.5\%$ (Fig. 10c) start to decorrelate. This decorrelation was more prominent at $\varepsilon_{a,\ mech} = 0.35$ (Fig. 10f). At $\varepsilon_{a,\ mech} = 0.35\%$ (Fig. 10f), the precipitates also exhibit noticeable coarsening, with their size increasing from an initial 10-30 nm to more than 60 nm on average.

4. Discussion

4.1. Microstructure and deformation

The cyclic response of the C263 nickel-based superalloy is influenced by its initial microstructure (Fig. 3), the applied loading mode, and the evolution of the dislocation substructure during TMF and isothermal IF fatigue (Fig. 9 and Fig. 10). Both TMF-IP and TMF-OP loading modes exhibited an initial hardening phase followed by saturation (Fig. 6a, b). However, there are several distinctions. For a comparable mechanical strain amplitude (e.g.0.5%), the TMF-OP test produced a stress amplitude approximately 100 MPa higher than that observed under TMF-IP conditions, highlighting the pronounced role of the loading phase on cyclic behaviour. Generally, the key contributing factors to the cyclic strengthening of nickel-based alloys are dislocation multiplication, dislocation interactions, and dislocation-precipitate interactions, as described by several authors [17,29,30]. Dislocation density evaluation for selected mechanical strain amplitudes of 0.5% and 0.35% (Fig. 10) showed that the TMF-OP condition consistently exhibited a higher dislocation density than the TMF-IP condition. This aligns with higher measured stresses in TMF-OP tested samples (Fig. 6a, b). The different deformation behaviour between TMF-OP and TMF-IP tested specimens was observed in other studies [16,38]. Higher cyclic stresses under TMF-OP are an effect of phase angle as explained by Mackay and Sangid [39] via crystal plasticity modelling on coarse grained polycrystalline nickel-based superalloy. Under TMF-IP loading, when the maximum

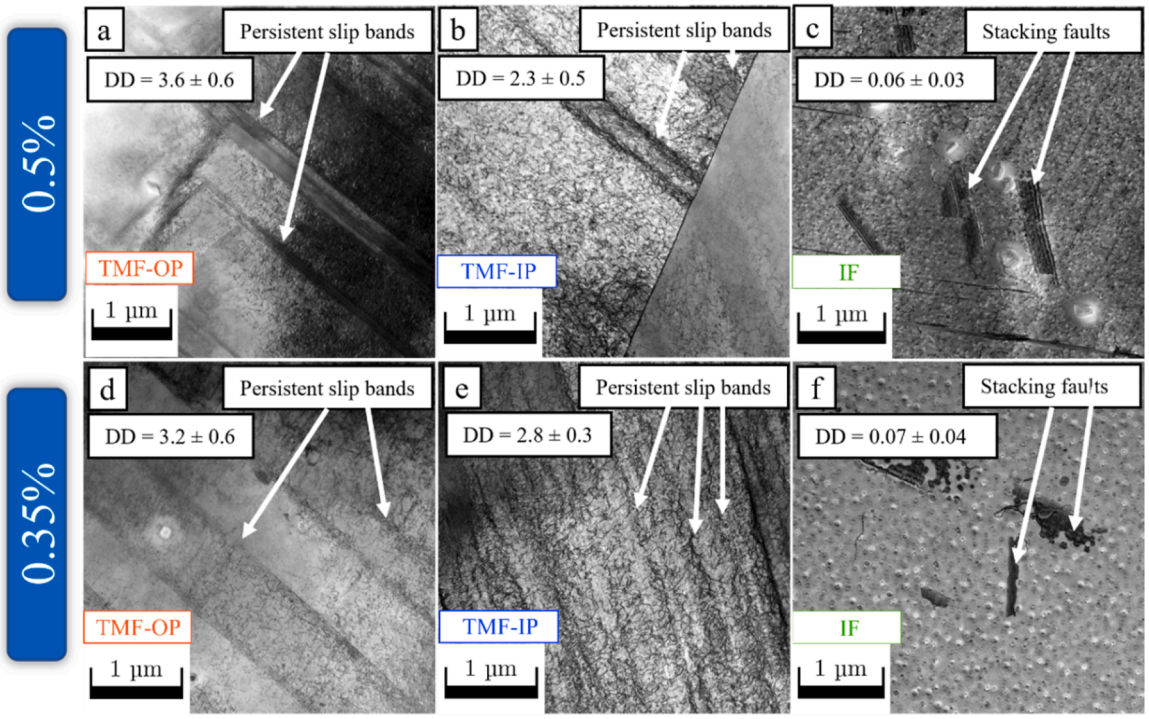

Fig. 10. STEM micrographs of dislocation structures (DD - Dislocation density is in 10^{14} m^{-2}) (a) TMF-OP, $\varepsilon_{a,\ mech} = 0.5\%$ (b) TMF-IP, $\varepsilon_{a,\ mech} = 0.5\%$; (c) IF, $\varepsilon_{a,\ mech} = 0.5\%$; (d) TMF- OP, $\varepsilon_{a,\ mech} = 0.35\%$; e) TMF-IP, $\varepsilon_{a,\ mech} = 0.35\%$; (f) IF, $\varepsilon_{a,\ mech} = 0.35\%$.

tensile load occurs at maximum temperature, reducing plastic flow stress and material stiffness lead to lower damage. Unlike the TMF-OP loading, when maximum tensile loading occurs at minimum temperature, stiffness and slip resistance, leading to higher micromechanical stress, greater slip system activity, a lower grain strength to stiffness ratio, and higher geometrically necessary dislocation density, which work well with experimental observations (Fig. 10). Other influencing factor is tension/compression asymmetry of yield and creep strength in nickel-based superalloys, not directly discussed in Mackay's et al. work [39]. Although C263 is polycrystalline, the presence of <111> texture with MUD > 2.4 (Fig. 3f) suggests that orientation-dependent asymmetry may develop, similar to that reported in single-crystal alloys by Tsuno et al. [40]. Tsuno et al. [40] investigated the differences in yield and creep strength development in tension and compression of 4 single crystal nickel-based superalloys within the range up to 900°C and attributed the tension/compression asymmetry to the directional formation of microtwins associated with the presence of stacking faults [40]. In our work, stacking faults were clearly observed in the initial condition (Fig. 3d) but were absent after TMF testing. At the same time, microtwins were present (Fig. 8f and Fig. 9b) only after TMF testing. A stacking fault to microtwin transformation pathway was proposed by Unocic et al. [41], who suggested that matrix-initiated intrinsic stacking faults formed by the decorrelation of a/2⟨110⟩ dislocations can, through repeated cross-slip and dissociation events, generate superlattice extrinsic stacking faults in the γ' phase via reorder-mediated shearing, which subsequently thicken the stacking fault into a microtwin. This statement also aligns with more recent high-resolution STEM observations [42], which provided direct atomic-scale evidence of transitional structures between superlattice extrinsic stacking faults and microtwins entirely within the γ' phase, validating the Kolbe [43] atomic rearrangement mechanism. Taken together, these findings support the interpretation that, under TMF loading, the stacking faults present in the initial microstructure can evolve into microtwins via sequential Shockley partial dislocation shearing, thereby linking the observed microstructural state to the tension/compression asymmetry mechanism investigated by [40] and observed in the different stress-strain response under TMF-OP and TMF-IP loading (Fig. 6a, b). The evolution of stacking faults into microtwins reduces the effectiveness of γ' as obstacles, since twin propagation allows cooperative shearing of both γ and γ' phases and provides a low-energy pathway for dislocation motion [41]. This facilitates localised deformation and promotes cyclic softening.

The development of the dislocation substructure varied significantly between TMF and IF tested specimens. The early stage of hardening in IF and TMF, shown in Fig. 6a, b, can be attributed to dislocation multiplication, dislocation-precipitate interaction, and the formation of dense dislocation tangles (Fig. 8) [44]. Another contributing strengthening mechanism commonly linked with a higher degree of hardening is DSA [45], which was observed under TMF loading (see hysteresis loops in Fig. 5a, b). These mechanisms increase internal resistance to plastic deformation. After the initial hardening, in the TMF tested specimen, the dislocation substructure rearranges, leading to the formation of dislocation-rich slip bands (Fig. 10a, b) and (Fig. 10d, e), observed also in [46,47]. In TMF tested polycrystalline C263, the formation of dislocation substructures (Fig. 9d) subdivides grains into microvolumes with different critical internal stresses. As shown by Polák and Šulák [48], an increasing fraction of plasticised microvolumes contributes to an increase in the macroscopic effective stress. The high dislocation densities observed in Fig. 10a–d are consistent with this interpretation and correlate with the elevated stress response during TMF. However, dislocation reorganisation leads to a redistribution of cyclic plastic strain, with dislocations preferentially gliding in the relatively soft persistent slip bands, thereby promoting cyclic softening [49,50]. Additionally, comparison of the initial microstructure (Fig. 3d) with the post-test microstructures (Fig. 9a–f) shows that the initially present stacking faults disappear. The combined effects of PSB formation, Shockley pair recombination, and subsequent annihilation act to counterbalance the hardening mechanisms associated with dislocation–precipitate interactions, dislocation entanglements, and dislocation interaction with planar faults. This interplay results in the saturation stage observed in the cyclic stress amplitude response during TMF loading (Fig. 6a, b). Unlike the TMF tested specimens, the IF tested specimens, after initial hardening, exhibited gradual softening over the

majority of the fatigue life, which is shown in Fig. 6c. It can be attributed to mechanisms such as dislocation climb, dislocation annihilation, and possible precipitate shearing (Fig. 9h) as also observed in Superni C263 in [30], and results in the lowest dislocation density among all employed loading cycles (Fig. 10). At lower strain amplitudes under IF loading, precipitate coarsening was more prevalent, attributable to prolonged exposure at 800 °C. This coarsening, combined with the decorrelation of Shockley partial dislocations inside stacking faults (Fig. 10c, f), led to the shearing of γ′ precipitates, similar to that proposed in [51]. The shearing mechanism that occurs after Shockley partial decorrelation is a contributing factor to the enhanced softening observed at a strain amplitude of 0.35%, where decorrelation is more pronounced (Fig. 10f).

4.2. The damage and lifetime behaviour

The reduced fatigue life under TMF loading is associated primarily with the prevailing crack initiation and propagation mechanisms, which differ between TMF-IP and TMF-OP conditions [10,52]. Specimens exposed to the TMF-IP cycle predominantly exhibited intergranular cracking (Fig. 8a–c), in contrast to those tested under TMF-OP conditions, where fatigue fracture was mainly transgranular (Fig. 8d–f). Intergranular cracking is generally associated with faster crack propagation and consequently reduced fatigue life [53]. This is commonly attributed to grain boundary weakening, which may occur through multiple mechanisms. These include grain boundary sliding under creep conditions, as observed in TMF-IP tested specimens by Guth [13], and also oxidation-assisted grain boundary decohesion [54], and the interaction of persistent slip bands with grain boundaries, as described by Mughrabi and Polák [55,56]. Evidence of wedge-type intergranular cracking, often linked to creep damage [57], is visible in the TMF-IP specimens (Fig. 8c), indicating that time-dependent deformation contributes to crack initiation and early crack propagation. This behaviour is consistent with the thermomechanical loading condition, where the maximum temperature coincides with maximum tensile strain, promoting creep deformation and grain boundary weakening, thereby facilitating intergranular crack propagation and shorter fatigue life. In contrast, TMF-OP specimens did not show typical features of creep damage but rather signs of oxidation-assisted crack initiation at the specimen surface. This is particularly evident in Fig. 11, where the crack appears to initiate from oxidised persistent slip marking, supporting the role of environmental effects during the tensile phase of the TMF-OP cycle. This observation is consistent with the findings of Petráš [9,52] who attributed crack initiation under TMF-OP conditions to cracking of a thick surface oxide layer, with repeated localised oxidation and oxide cracking leading to transgranular crack growth. The relative contributions of crack initiation and propagation to total fatigue life are not universal but depend on the material, loading conditions, and environmental effects. In high-temperature fatigue, especially under LCF [58] and TMF [59] conditions, a substantial part of fatigue life may be associated with the growth of short cracks.

Dynamic recrystallisation was observed in the form of very fine grain nucleation along grain boundaries in TMF-OP (Fig. 8f), TMF-IP (Fig. 8c), and also in IF (Fig. 8i) tested specimens, whereas such features were absent in the initial state. This phenomenon is consistent with local grain-boundary bulging previously reported for Ni–Cr alloys [60]. Dislocation cell structures develop preferentially along grain boundaries (Fig. 12c), where progressive recovery promotes subgrain formation, which subsequently evolves into fine recrystallised grains (Fig. 12d). These recrystallised grains remain localised near the boundaries (Fig. 12a, b). Moreover, high stress concentrations ahead of crack tips promote rapid dislocation cell formation and accelerate subgrain development and local recrystallisation (Fig. 12b), consistent with observations reported by Polák et al. [61]. In nickel-based superalloys, multiple authors have reported dynamic recrystallisation [62,63], though often due to high-temperature exposure during post-deformation heat treatment rather than under in-service mechanical loading. Under IF conditions, dynamic recrystallisation was recently reported for ODS steel exposed to fatigue loading at 1000 °C and 1200 °C [64]. Moverare [65] demonstrated that in the single-crystal superalloy CMSX-4, recrystallisation can occur under TMF-OP cycling between 100–1000 °C. In both cases, this process was driven by cyclic plastic deformation and the associated recovery mechanisms at high temperature. In contrast to these studies, dynamic recrystallisation was observed in the present work in the polycrystalline nickel-based superalloy C263 at comparatively lower temperatures, with a maximum temperature of 800 °C. This behaviour can be partly attributed to the relatively low volume fraction of γ′ precipitates in C263, which was estimated to be approximately 10 % up to 800 °C [66], in contrast to high-γ′ superalloys such as CMSX-4 [67] or CM247LC [68]. γ′ precipitates act as effective obstacles to dislocation motion. Therefore, a high precipitate volume fraction increases alloy strength by restricting dislocation glide and reducing the extent of plastic deformation. In C263, the lower density of γ′ precipitates allows a larger fraction of the imposed cyclic strain to be accommodated by plastic deformation. Another contributing factor may

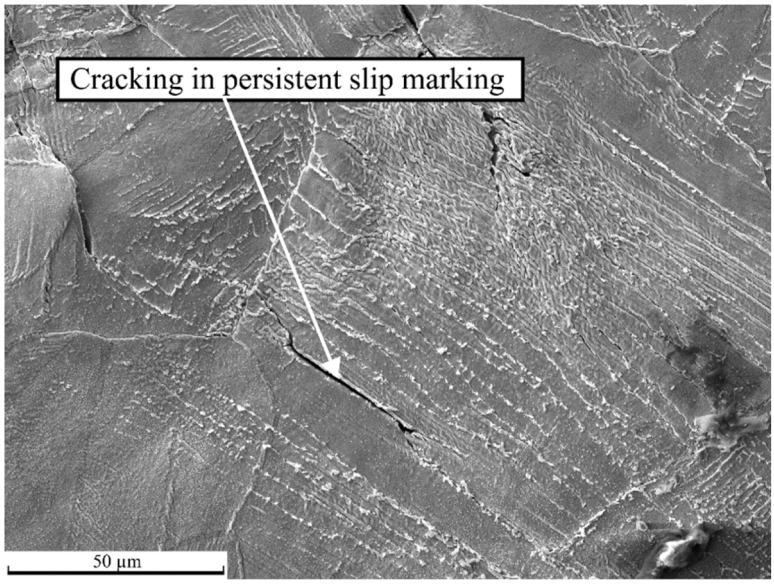

Fig. 11. Fatigue crack initiation from PSM under TMF-OP loading.

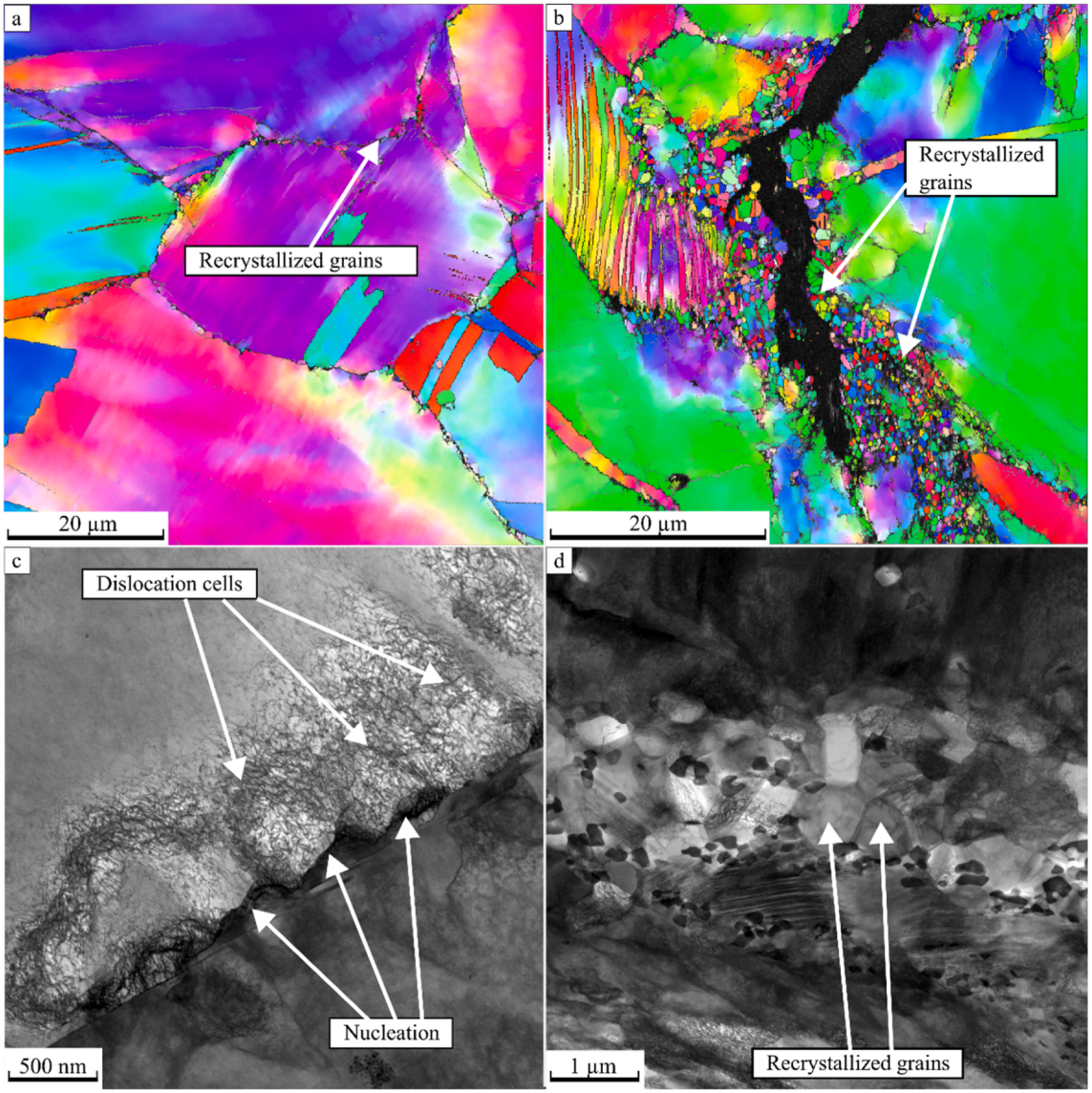

Fig. 12. Dynamic recrystallization in TMF-OP tested specimen with $\varepsilon_{a,\ mech} = 0.5\%$; a) EBSD grain orientation map with recrystalized grains along the grain boundaries; b) EBSD grain orientation map displaying recrystallization along the crack path; c) STEM micrograph of dislocation cell formation and subsequent nucleation within grain boundary; d) STEM micrograph of recrystallized grains.

be the relatively low stacking fault energy of C263 as reported by Galindo-Nava et al. [68]. The relatively low stacking fault energy is associated with the tendency of Co additions to reduce the stacking fault energy in Ni–Cr solid solutions [69]. Reduced stacking fault energy limits cross-slip and dynamic recovery, promotes planar slip, and favours the localisation of cyclic plastic deformation into persistent slip bands. When persistent slip bands interact with grain boundaries, local stress concentration may facilitate fine grain nucleation. Importantly, in TMF-OP, dynamic recrystallisation was not confined only to crack-tip regions, as observed in IF and TMF-IP, but fine recrystallised grains were also detected along grain boundaries outside of the vicinity of secondary cracks (Fig. 12a, c, d). A potential explanation is that under IF conditions, recovery at elevated temperature promotes dislocation annihilation and reduces the amount of statistically stored dislocations in the matrix (Fig. 10c, f). As a result, dynamic recrystallisation is largely restricted to regions experiencing the highest plastic strain, i.e., near crack tips. Although the plastic strain amplitudes at half of the lifetime in TMF-IP were comparable to those in TMF-OP (Table 3), dynamic recrystallisation outside the crack-tip zone was not observed in TMF-IP. It is hypothesised that in TMF-IP, the coincidence of maximum tensile strain with maximum temperature promotes early grain-boundary damage and accelerates strain localisation at crack tips. Consequently, the dominant fraction of cyclic plasticity is accommodated in the immediate vicinity of the crack tip. In contrast, in TMF-OP, the maximum temperature coincides with compressive loading, which suppresses grain-boundary opening and delays crack propagation. This condition prolongs the stage during which plastic deformation is distributed over a larger material volume, with preferential localisation in grains with high Schmid factors. Such conditions facilitate gradual subgrain development and enable dynamic recrystallisation along grain boundaries outside the crack-tip zone. The formation of newly recrystallised fine grains in the material can increase the yield strength and may contribute to the pronounced strengthening observed in Fig. 6b via grain-boundary strengthening from grain refinement, as expressed by the Hall–Petch Eq., and confirmed by Hadraba et al. [70] to remain applicable even for bimodal microstructures. Although recrystallisation is more prominent in TMF-OP, its effect on lifetime is less severe than in IF or TMF-IP, as crack propagation is primarily transgranular. Nevertheless, as shown in Fig. 8f, although the crack is mainly transgranular, the presence of newly recrystallised fine grains along boundaries can locally deflect the

crack path and promote partial intergranular propagation, which may reduce the lifetime compared to purely transgranular cracking.

Zhang et al. [18] reported dynamic recrystallisation in C263 under TMF-OP loading conditions in the temperature range of 300–950 °C, supporting the hypothesis that recrystallisation during TMF testing can contribute to intergranular crack initiation, which aligns with findings in Fig. 8. The authors further demonstrated that selecting the maximum temperature in a TMF cycle to 950 °C leads to a lower lifetime during TMF-OP relative to TMF-IP in C263 [18], which seems to disagree with our results. However, this difference is likely related to the substantially higher maximum temperature used in [18]. At temperatures approaching 900–950 °C, the strengthening effect of γ' precipitates is reduced due to their gradual dissolution, while carbides may partially dissolve and coarsen [33], reducing their ability to pin grain boundaries and suppress creep-related deformation. As a result, creep-assisted damage and oxidation become markedly more pronounced at 950 °C than at 800 °C, which can promote severe surface degradation and extensive intergranular cracking during the tensile half-cycle of TMF-OP loading. Moreover, the statistical scatter inherent in TMF data, as well as the limitations of testing only a single specimen per condition and different strain rates, should be carefully considered.

The Manson–Coffin curve (Fig. 4b) indicates a higher plastic strain contribution in the C263 specimen tested at 800 °C, while the Basquin curve (Fig. 4c) demonstrates a pronounced reduction in fatigue life at the lowest strain amplitude levels compared with [30]. This reduction can be attributed to the temperature-dependent decrease in the critical resolved shear stress, which facilitates dislocation climb and cross-slip. Comparing our results with those of Zhang and Knowles [18] and Dinesh et al. [30] shows that the cycle period is an important lifetime factor. This study applied a loading cycle with a period of 100 s, while [30] used 5-20 s and [18] employed the shortest period of 4s. The IF life curve obtained in this work (Fig. 4a) exhibits the steepest slope, followed by that from [30], with [18] showing the shallowest. Clearly, the slope steepness correlates with increasing cycle period. Such frequency sensitivity has been observed in other nickel-based alloys. Organ et al. [71] reported that for wrought Udimet 700 tested at 760 °C, fatigue life was highest at cycle period $T = 0.1$ s and decreased at higher cycle periods $T > 60$ s, primarily due to enhanced creep and oxidation at grain boundaries. Low-frequency cycling promoted intergranular crack initiation at surface-connected grain boundaries, followed by crack propagation along weakened paths. Similarly, Tsuji and Kondo [72] demonstrated that in Hastelloy X and XR tested at 900 °C, a slower strain rate led to a marked decrease in fatigue life due to creep-assisted intergranular crack initiation and cavity formation along grain boundaries. A similar trend was confirmed in MAR-247 by Šulák et al. [73], where lower strain rates reduced fatigue life and also shifted the crack propagation mechanism from transgranular to a mixed transgranular and intergranular mode. Under IF loading, a mixed transgranular and intergranular fracture mode of fatigue crack propagation was observed (Fig. 8), in contrast to the predominantly transgranular cracking reported by Zhang and Knowles [18]. The mixed mode of cracking can be attributed to the significantly longer cycle period applied in the present study, which promotes time-dependent damage. However, the purely intergranular cracking reported by Dinesh et al. [30] cannot be rationalised by the cycle period effect, as their cycle period was substantially shorter. A key difference may lie in different manufacturing procedures and the Mo content, which is approximately 0.8 wt.% lower in Superni-263. This reduced Mo content may render grain boundaries more susceptible to creep damage, considering that Mo contributes to the formation and stability of $M_{23}C_6$ carbides along grain boundaries (Fig. 3a).

5. Conclusion

This study provides microstructural and fractographical analysis of the polycrystalline nickel-based superalloy C263 cyclically loaded under TMF-IP, TMF-OP loading in the temperature range of 300-800°C, and under IF loading at the constant temperature of 800°C. The following conclusions can be drawn:

1. The fatigue life of the C263 superalloy followed the order TMF-OP > IF > TMF-IP, with the shortest life in TMF-IP attributed to the damaging coincidence of peak strain and peak temperature. The observed lifetime ranking reflects the dominant crack propagation modes: transgranular in TMF-OP, mixed transgranular–intergranular in IF, and predominantly intergranular in TMF-IP, the latter being the most detrimental.
2. The stress amplitudes under OP-loading exceed those for IP-loading, since the yield strength at maximum temperature is higher under compressive loading than under tensile loading. This tension–compression asymmetry may be related to a slight ⟨111⟩ texture and can be further enhanced by recrystallisation of fine grains during cycling.
3. Dynamic recrystallisation occurred during both TMF and IF cycling. At high stress amplitudes, dislocation reorganisation promoted subgrain formation and the nucleation of new grains, most prominently under TMF-OP, while stresses under the crack-tip further accelerated recrystallisation. The newly generated grain boundaries offer a preferred crack path under TMF-IP and IF loading, presumably reducing the lifetime.
4. The softening mechanism of C263 alloy under isothermal fatigue at 800 °C was linked to the lowest dislocation density among all loading modes, attributed to mechanisms such as dislocation climb, annihilation, and γ' precipitate shearing. At lower strain amplitudes, prolonged high-temperature exposure promoted γ' coarsening and the decorrelation of Shockley partials inside pre-existing stacking faults, further facilitating precipitate shearing.

CRediT authorship contribution statement

Tomáš Vražina: Writing – original draft, Methodology, Investigation, Formal analysis, Data curation, Conceptualization. **Stefan Guth:** Writing – review & editing, Data curation, Conceptualization. **Ladislav Poczklán:** Methodology, Data curation, Conceptualization. **Jakub Poloprudský:** Writing – review & editing, Formal analysis, Data curation. **Markéta Gálíková:** Investigation, Formal analysis. **Tomáš Babinský:** Writing – review & editing, Investigation, Data curation. **Daniel Petrell:** Writing – review & editing, Resources. **Benedikt Nowak:** Writing – review & editing, Resources. **Ivo Šulák:** Writing – review & editing, Visualization, Supervision, Resources, Methodology, Conceptualization.

Declaration of competing interest

The authors declare that they have no known competing financial interests or personal relationships that could have appeared to influence the work reported in this paper.

Acknowledgement

This publication was supported by the project "Mechanical Engineering of Biological and Bio-inspired Systems", funded as project No. CZ.02.01.01/00/22_008/0004634 by Programme Johannes Amos Comenius, call Excellent Research and by the project INTER-COST, grant no. LUC24093, awarded by the Ministry of Education, Youth and Sports of the Czech Republic. Support from the Czech Academy of Sciences under the Lumina quaeruntur project is greatly appreciated. The authors would also like to thank VDM Metals International GmbH for providing the material for this research. We acknowledge CzechNanoLab Research Infrastructure (ID 90251), supported by MEYS CR.

Data availability

https://doi.org/10.5281/zenodo.1802282 (Data are available at)

References

[1] B. Tramošljika, P. Blecich, I. Bonefačić, V. Glažar, Advanced ultra-supercritical coal-fired power plant with post-combustion carbon capture: analysis of electricity penalty and CO2 emission reduction, Sustainability 13 (2021) 801, https://doi.org/10.3390/su13020801.

[2] A.D. Gianfrancesco, Materials for Ultra-Supercritical and Advanced Ultra-Supercritical Power Plants, Woodhead Publishing, 2016.

[3] D. Wang, L. Chen, Y. Zhao, W. Chen, C. Wang, J. Yan, Thermomechanical stress analysis and fatigue lifetime evaluation of coal-fired boiler components during peak shaving transient processes: Effects of load cycling rate, Int. J. Press. Vessels Pip. 206 (2023) 105083, https://doi.org/10.1016/j.ijpvp.2023.105083.

[4] P. Yin, W. Zhang, S. Guo, J. Wen, G. Zhang, F. Xue, Y. Zhao, C. Zhou, Thermomechanical fatigue behaviour and damage mechanisms in a 9% Cr steel: Effect of strain rate, Mater. Sci. Eng.: A 815 (2021) 141308, https://doi.org/10.1016/j.msea.2021.141308.

[5] G.R. Halford, M.A. McGaw, R.C. Bill, P.D. Fanti, Bithermal Fatigue: A Link Between Isothermal and Thermomechanical Fatigue, (1988). https://doi.org/10.1520/STP24510S.

[6] I. Šulák, K. Obrtlík, Thermomechanical and isothermal fatigue properties of MAR-M247 superalloy, Theor. Appl. Fract. Mech. 131 (2024) 104443, https://doi.org/10.1016/j.tafmec.2024.104443.

[7] W. Deng, J. Xu, Y. Hu, Z. Huang, L. Jiang, Isothermal and thermomechanical fatigue behavior of Inconel 718 superalloy, Mater. Sci. Eng.: A 742 (2019) 813–819, https://doi.org/10.1016/j.msea.2018.11.052.

[8] I. Šulák, K. Obrtlík, The effect of dwell on thermomechanical fatigue behaviour of Ni-base superalloy Inconel 713LC, Int. J. Fatigue 166 (2023) 107238, https://doi.org/10.1016/j.ijfatigue.2022.107238.

[9] R. Petráš, V. Škorík, J. Polák, Thermomechanical fatigue and damage mechanisms in Sanicro 25 steel, Mater. Sci. Eng.: A 650 (2016) 52–62, https://doi.org/10.1016/j.msea.2015.10.030.

[10] S. Guth, K.-H. Lang, Influence of dwell times on microstructure, deformation and damage behavior of NiCr22Co12Mo9 under thermomechanical fatigue, Mater. Sci. Eng.: A 794 (2020) 139970, https://doi.org/10.1016/j.msea.2020.139970.

[11] R.J. Lancaster, M.T. Whittaker, S.J. Williams, A review of thermo-mechanical fatigue behaviour in polycrystalline nickel superalloys for turbine disc applications, Mater. High Temp. 30 (2013) 2–12, https://doi.org/10.3184/096034013.13630238172260.

[12] M. Segersäll, D. Deng, A comparative study between in- and out-of-phase thermomechanical fatigue behaviour of a single-crystal superalloy, Int. J. Fatigue 146 (2021) 106162, https://doi.org/10.1016/j.ijfatigue.2021.106162.

[13] S. Guth, K.-H. Lang, An approach to lifetime prediction for a wrought Ni-base alloy under thermo-mechanical fatigue with various phase angles between temperature and mechanical strain, Int. J. Fatigue 99 (2017) 286–294, https://doi.org/10.1016/j.ijfatigue.2016.10.015.

[14] G.V. Prasad Reddy, A. Nagesha, R. Sandhya, S. Sankaran, M.D. Mathew, K. Bhanu Sankara Rao, Thermomechanical and isothermal fatigue behavior of 316LN stainless steel with varying nitrogen content, Met. Mater. Trans. A 46 (2015) 695–707, https://doi.org/10.1007/s11661-014-2653-y.

[15] A. Nagesha, M. Valsan, R. Kannan, K. Bhanu Sankara Rao, V. Bauer, H.-J. Christ, V. Singh, Thermomechanical fatigue evaluation and life prediction of 316L(N) stainless steel, Int. J. Fatigue 31 (2009) 636–643, https://doi.org/10.1016/j.ijfatigue.2008.03.019.

[16] I. Šulák, K. Hrbáček, K. Obrtlík, The Effect of Temperature and Phase Shift on the Thermomechanical Fatigue of Nickel-Based Superalloy, Metals 12 (2022) 993, https://doi.org/10.3390/met12060993.

[17] T. Babinský, I. Šulák, I. Kuběna, J. Man, A. Weiser, E. Švábenská, L. Englert, S. Guth, Thermomechanical fatigue of additively manufactured 316L stainless steel, Mater. Sci. Eng.: A 869 (2023) 144831, https://doi.org/10.1016/j.msea.2023.144831.

[18] Y.H. Zhang, D.M. Knowles, Isothermal and Thermomechanical Fatigue of Superalloy C263, in: Superalloys 2000 (Ninth International Symposium), TMS, 2000, pp. 545–552, https://doi.org/10.7449/2000/Superalloys_2000_545_552.

[19] L. Zhang, Z.W. Yu, L.C. Zhang, R. Jiang, L.G. Zhao, Y.D. Song, Thermo-mechanical fatigue deformation and fracture mechanisms of nickel-based powder metallurgy superalloy, Int. J. Fatigue 180 (2024) 108083, https://doi.org/10.1016/j.ijfatigue.2023.108083.

[20] R. Zauter, H.J. Christ, H. Mughrabi, Some aspects of thermomechanical fatigue of AISI 304L stainless steel: Part I. creep- fatigue damage, Met. Mater. Trans. A 25 (1994) 401–406, https://doi.org/10.1007/BF02647985.

[21] J.-C. Zhao, V. Ravikumar, A. Beltran, Phase Precipitation and Phase Stability in Nimonic 263, Metall. Mater. Trans. A-Phys. Metall. Mater. Sci. - Met. Mater. Trans. A 32 (2001) 1271–1282, https://doi.org/10.1007/s11661-001-0217-4.

[22] V.S. Bhattachar, Thermal fatigue behaviour of nickel-base superailoy 263 sheets, Int. J. Fatigue 17 (1995) 407–413, https://doi.org/10.1016/0142-1123(95)00006-F.

[23] K. Maile, Qualification of Ni-Based Alloys for Advanced Ultra Supercritical Plants, Procedia Eng. 55 (2013) 214–220, https://doi.org/10.1016/j.proeng.2013.03.245.

[24] A. Manonukul, F.P.E. Dunne, D. Knowles, S. Williams, Multiaxial creep and cyclic plasticity in nickel-base superalloy C263, Int. J. Plast. 21 (2005) 1–20, https://doi.org/10.1016/j.ijplas.2003.12.005.

[25] R. S S. Karthikeyan, V. Balasubramanian, S. Yishak, Evaluation of microstructure and mechanical properties of thermally sprayed NiCrAlY bond coats on Superni C-263 aero engine combustor liner alloy, Results Eng. 26 (2025) 105060, https://doi.org/10.1016/j.rineng.2025.105060.

[26] J. Jadav, K.V. Rajulapati, K.B.S. Rao, N.E. Prasad, R. Mythili, K. Prasad, Strain controlled isothermal low cycle fatigue life, deformation and fracture characteristics of Superni 263 superalloy, Mater. Sci. Eng.: A 760 (2019) 296–315, https://doi.org/10.1016/j.msea.2019.05.119.

[27] R. Pohja, A. Nurmela, null Holmström Stefan, P. Moilanen, Creep-fatigue properties of nickel-base superalloy 263: BALTICA IX - International Conference on Life Management and Maintenance for Power Plants, Baltica IX. International Conference on Life Management and Maintenance for Power Plants (2013) 204–217.

[28] V. Ratna, D.S. Sarma, Influence of thermal fatigue on the microstructure of a Ni-base superalloy, Scr. Metall. Mater. 29 (1993) 467–472, https://doi.org/10.1016/0956-716X(93)90149-M.

[29] K. Dinesh, B.B. Dash, R. Kannan, N. Paulose, G.V.P. Reddy, H. Krishnaswamy, S. Sankaran, Effect of strain amplitude on the low cycle fatigue behavior and deformation mechanisms in alloy SU-263 at elevated temperature, Mater. Sci. Eng.: A 920 (2025) 147518, https://doi.org/10.1016/j.msea.2024.147518.

[30] K. Dinesh, B.B. Dash, R. Kannan, N. Paulose, G.V. Prasad Reddy, H. Krishnaswamy, S. Sankaran, Effect of temperature on fatigue behavior and deformation mechanisms of nickel-based superalloy SU-263, Int. J. Fatigue 192 (2025) 108721, https://doi.org/10.1016/j.ijfatigue.2024.108721.

[31] S.-G. Hong, S.-B. Lee, Mechanism of dynamic strain aging and characterization of its effect on the low-cycle fatigue behavior in type 316L stainless steel, J. Nucl. Mater. 340 (2005) 307–314, https://doi.org/10.1016/j.jnucmat.2004.12.012.

[32] I.S. Choi, S.W. Nam, K.-T. Rie, Mechanism of the fatigue life increment due to dynamic strain ageing during hold time, J. Mater. Sci. 20 (1985) 2446–2458, https://doi.org/10.1007/BF00556073.

[33] J. Hunfeld, H. Sommer, J. Kiese, H. Wang, A. Riyahi khorasgani, T. Li, C. Somsen, A. Kostka, G. Laplanche, Design of a new wrought CrCoNi-based medium-entropy superalloy C-264 for high-temperature applications, Mater. Des. 211 (2021) 110174, https://doi.org/10.1016/j.matdes.2021.110174.

[34] M. Shehata, Emissions and wall temperatures for lean prevaporized premixed gas turbine combustor, Fuel 88 (2009) 446–455, https://doi.org/10.1016/j.fuel.2008.10.031.

[35] P. Hähner, E. Affeldt, T. Beck, H. Klingelhöffer, M. Loveday, European Commission, in: C. Rinaldi (Ed.), Validated code-of-practice for strain-controlled thermo-mechanical fatigue testing, Publications Office, Luxembourg, 2006.

[36] Y. Meng, X. Ju, X. Yang, The measurement of the dislocation density using TEM, Mater. Charact. 175 (2021) 111065, https://doi.org/10.1016/j.matchar.2021.111065.

[37] Y.-U. Heo, Comparative study on the specimen thickness measurement using EELS and CBED methods, Appl. Microsc. 50 (2020) 8, https://doi.org/10.1186/s42649-020-00029-4.

[38] V.H. Dao, H.S. Yun, J.S. Koo, P. Jaeyeong, S.H. Nahm, Experimental investigation of thermomechanical fatigue behavior in directionally solidified Ni-based superalloy under in-phase and out-of-phase conditions, J. Alloys Compd. 990 (2024) 174430, https://doi.org/10.1016/j.jallcom.2024.174430.

[39] B.T. Mackey, M.D. Sangid, Phasing effects on thermo-mechanical fatigue damage investigated via crystal plasticity modeling, Mater. Sci. Eng.: A 903 (2024) 146642, https://doi.org/10.1016/j.msea.2024.146642.

[40] N. Tsuno, S. Shimabayashi, K. Kakehi, C.M.F. Rae, R.C. Reed, Tension/compression asymmetry in yield and creep strengths of Ni-based superalloys, Superalloys (2008) 433–442.

[41] R.R. Unocic, N. Zhou, L. Kovarik, C. Shen, Y. Wang, M.J. Mills, Dislocation decorrelation and relationship to deformation microtwins during creep of a γ′ precipitate strengthened Ni-based superalloy, Acta Mater. 59 (2011) 7325–7339, https://doi.org/10.1016/j.actamat.2011.07.069.

[42] X. Li, H. Zhang, J. Jia, J. Liu, Y. Zhang, A twinning mechanism: Direct observation of the transition from stacking faults to Microtwins, Scr. Mater. 267 (2025) 116803, https://doi.org/10.1016/j.scriptamat.2025.116803.

[43] M. Kolbe, The high temperature decrease of the critical resolved shear stress in nickel-base superalloys, Mater. Sci. Eng.: A 319–321 (2001) 383–387, https://doi.org/10.1016/S0921-5093(01)00944-3.

[44] R.E. Stoltz, A.G. Pineau, Dislocation-precipitate interaction and cyclic stress-strain behavior of a γ′ strengthened superalloy, Mater. Sci. Eng. 34 (1978) 275–284, https://doi.org/10.1016/0025-5416(78)90060-5.

[45] Ch.V. Rao, N.C.S. Srinivas, G.V.S. Sastry, V. Singh, Dynamic strain aging, deformation and fracture behaviour of the nickel base superalloy Inconel 617, Mater. Sci. Eng.: A 742 (2019) 44–60, https://doi.org/10.1016/j.msea.2018.10.123.

[46] P. Yin, W. Zhang, Y. Zhang, Q. Yang, F. Liang, L. Chang, C. Zhou, Cyclic deformation mechanism and fracture behaviour of 316L stainless steel under thermomechanical fatigue loading, J. Mater. Res. Technol. 24 (2023) 4484–4499, https://doi.org/10.1016/j.jmrt.2023.04.113.

[47] I. Šulák, K. Obrtlík, AFM, SEM AND TEM study of damage mechanisms in cyclically strained mar-M247 at room temperature and high temperatures, Theor. Appl. Fract. Mech. 108 (2020) 102606, https://doi.org/10.1016/j.tafmec.2020.102606.

[48] J. Polák, I. Šulák, Effective and internal stresses in cyclically strained materials, Results Eng. 25 (2025) 103895, https://doi.org/10.1016/j.rineng.2024.103895.

[49] L.M. Brown, Dislocation plasticity in persistent slip bands, Mater. Sci. Eng.: A 285 (2000) 35–42, https://doi.org/10.1016/S0921-5093(00)00662-6.
[50] H. Mughrabi, The cyclic hardening and saturation behaviour of copper single crystals, Mater. Sci. Eng. 33 (1978) 207–223, https://doi.org/10.1016/0025-5416(78)90174-X.
[51] B. Décamps, S. Raujol, A. Coujou, F. Pettinari-Sturmel, N. Clément, D. Locq, P. Caron, On the shearing mechanism of γ′ precipitates by a single ⟨a/6⟩⟨112⟩ Shockley partial in Ni-based superalloys, Philos. Mag. 84 (2004) 91–107, https://doi.org/10.1080/14786430310001621472.
[52] R. Petráš, I. Šulák, J. Polák, The effect of dwell on thermomechanical fatigue in superaustenitic steel Sanicro 25, Fatigue Fract. Eng. Mater. Struct. 44 (2021) 673–688, https://doi.org/10.1111/ffe.13385.
[53] S. Eckmann, C. Schweizer, Characterization of fatigue crack growth, damage mechanisms and damage evolution of the nickel-based superalloys MAR-M247 CC (HIP) and CM-247 LC under thermomechanical fatigue loading using in situ optical microscopy, Int. J. Fatigue 99 (2017) 235–241, https://doi.org/10.1016/j.ijfatigue.2017.01.015.
[54] R. Molins, G. Hochstetter, J.C. Chassaigne, E. Andrieu, Oxidation effects on the fatigue crack growth behaviour of alloy 718 at high temperature, Acta Mater. 45 (1997) 663–674, https://doi.org/10.1016/S1359-6454(96)00192-9.
[55] H. Mughrabi, A Model of High-Cycle Fatigue-Crack Initiation at Grain Boundaries by Persistent Slip Bands, in: G.C. Sih, J.W. Provan (Eds.), Defects, Fracture and Fatigue, Springer Netherlands, Dordrecht, 1983, pp. 139–146, https://doi.org/10.1007/978-94-009-6821-9_11.
[56] J. Polák, T. Babinský, T. Vražina, T. Kruml, Mechanism of intergranular fatigue crack growth in copper polycrystal, Int. J. Fatigue 182 (2024) 108190, https://doi.org/10.1016/j.ijfatigue.2024.108190.
[57] M. Tanaka, H. Iizuka, On the initiation of wedge-type cracks at grain-boundary triple junctions during high-temperature creep, J. Mater. Sci. 20 (1985) 9–16, https://doi.org/10.1007/BF00555892.
[58] V. Mazánová, J. Polák, Initiation and growth of short fatigue cracks in austenitic Sanicro 25 steel, Fatigue Fract. Eng. Mater. Struct. 41 (2018) 1529–1545, https://doi.org/10.1111/ffe.12794.
[59] N. Leost, D. Missoum-Benziane, M. Rambaudon, L. Cameriano, F. Comte, B. Le Pannerer, V. Maurel, Short fatigue crack growth sensitivity to thermo-mechanical fatigue loading, Int. J. Fatigue 191 (2025) 108651, https://doi.org/10.1016/j.ijfatigue.2024.108651.
[60] N. Dudova, A. Belyakov, T. Sakai, R. Kaibyshev, Dynamic recrystallization mechanisms operating in a Ni–20%Cr alloy under hot-to-warm working, Acta Mater. 58 (2010) 3624–3632, https://doi.org/10.1016/j.actamat.2010.02.032.
[61] J. Polák, L. Poczklán, T. Vražina, Dislocation Structure Near the Intergranular Fracture Surface of Cyclically Strained Polycrystalline Copper, Fatigue Fract. Eng. Mater. Struct. 48 (2025) 3110–3121, https://doi.org/10.1111/ffe.14663.
[62] B. Zhang, X. Lu, D. Liu, C. Tao, Influence of recrystallization on high-temperature stress rupture property and fracture behavior of single crystal superalloy, Mater. Sci. Eng.: A 551 (2012) 149–153, https://doi.org/10.1016/j.msea.2012.04.109.
[63] Q. Yang, Y. Li, F. Wang, J. Wang, D. Li, J. Wu, Effect of surface recrystallization on high-temperature tensile properties of a directionally solidified DZ409 Ni-based superalloy, China Foundry 22 (2025) 463–470, https://doi.org/10.1007/s41230-025-4265-0.
[64] I. Šulák, A. Chlupová, J. Poloprudský, J. Svoboda, Cyclic plastic response of rotary swaged Fe-14Cr-10Al-4Y2O3 ODS alloy at 1000–1200 °C, Mater. Charact. 207 (2024) 113519, https://doi.org/10.1016/j.matchar.2023.113519.
[65] J.J. Moverare, S. Johansson, R.C. Reed, Deformation and damage mechanisms during thermal–mechanical fatigue of a single-crystal superalloy, Acta Mater. 57 (2009) 2266–2276, https://doi.org/10.1016/j.actamat.2009.01.027.
[66] G. Angella, R. Donnini, D. Ripamonti, M. Maldini, The role of particle ripening on the creep acceleration of Nimonic 263 superalloy, MATEC Web Conf. 14 (2014) 14001, https://doi.org/10.1051/matecconf/20141414001.
[67] R.D. Jones, F. Di Gioacchino, H. Lim, T.E.J. Edwards, C. Schwalbe, C.C. Battaile, W. J. Clegg, Reduced partitioning of plastic strain for strong and yet ductile precipitate-strengthened alloys, Sci. Rep. 8 (2018) 8698, https://doi.org/10.1038/s41598-018-26917-0.
[68] E.I. Galindo-Nava, R. Schlütter, O.M.D.M. Messé, C. Argyrakis, C.M.F. Rae, A model for dislocation creep in polycrystalline Ni-base superalloys at intermediate temperatures, Int. J. Plast. 169 (2023) 103729, https://doi.org/10.1016/j.ijplas.2023.103729.
[69] F. Pettinari, J. Douin, G. Saada, P. Caron, A. Coujou, N. Clément, Stacking fault energy in short-range ordered γ-phases of Ni-based superalloys, Mater. Sci. Eng.: A 325 (2002) 511–519, https://doi.org/10.1016/S0921-5093(01)01765-8.
[70] H. Hadraba, L. Stratil, F. Siska, Z. Chlup, L. Bertolla, E. Siska Viragova, M. Vilemova, Strengthening 316L austenitic steel through a bimodal approach with ODS steel, J. Mater. Sci. 60 (2025) 17971–17988, https://doi.org/10.1007/s10853-025-11444-x.
[71] F.E. Organ, M. Gell, The effect of frequency on the elevated temperature fatigue of a nickel-base superalloy, Met. Trans. 2 (1971) 943–952, https://doi.org/10.1007/BF02664223.
[72] H. Tsuji, T. Kondo, Strain-time effects in low-cycle fatigue of nickel-base heat-resistant alloys at high temperature, J. Nucl. Mater. 150 (1987) 259–265, https://doi.org/10.1016/0022-3115(87)90002-X.
[73] I. Šulák, K. Obrtlík, T. Babinský, S. Guth, The low cycle fatigue behaviour of MAR-M247 superalloy under different strain rates and cycle shapes at 750 °C, Int. J. Fatigue 164 (2022) 107133, https://doi.org/10.1016/j.ijfatigue.2022.107133.